# Ion irradiation of acetylene ice in the ISM and the outer Solar system: laboratory simulations

R. C. Pereira,[1] A. L. F. de Barros [ORCID],[1,2]★ C. A. P. da Costa,[3] P. R .B. Oliveira,[3] D. Fulvio [ORCID][3]† and E. F. da Silveira[3]★

[1]*Programa de Pós-graduação em Instrumentação e Óptica Aplicada, Centro Federal de Educação Tecnológica Celso Suckow da Fonseca, Av. Maracanã 229, 20271-110 Rio de Janeiro, RJ, Brazil*
[2]*Departamento de Física, Centro Federal de Educação Tecnológica Celso Suckow da Fonseca, Av. Maracanã 229, 20271-110 Rio de Janeiro, RJ, Brazil*
[3]*Departamento de Física, Pontifícia Universidade Católica do Rio de Janeiro, Rua Marquês de São Vicente 225, 22451-900 Rio de Janeiro, RJ, Brazil*

## ABSTRACT)3

Acetylene, $C_2H_2$, has been observed in the interstellar medium, mostly around young stellar objects, as well as in molecular clouds and cometary comae, representing an important species of astrophysical interest. In this work, we present a laboratory study of the $C_2H_2$ radiolysis at 45 K for three different beams and energies: 1.0 MeV $H^+$ and $He^+$, and 1.0 and 1.5 MeV $N^+$ beams. Fourier transform infrared spectroscopy was used for monitoring the molecular changes induced by the ion processing. Two different sample thicknesses were irradiated; for the thicker one, implantation had occurred. Spectra and absorbance evolutions for the thin and thick films are qualitatively different. Four $C_2H_2$ bands are observed at 3225, 1954, 1392, and 763 cm$^{-1}$. The $C_2H_2$ compaction and apparent destruction cross-sections are determined. For the case of the $H^+$ beam, the compaction cross-section dominates. Concerning molecular synthesis by irradiation, New product bands were not observed in the thin ice irradiations; for the thicker film ice, the daughter species $CH_4$, $C_2H_4$, $C_3H_6$, and $C_4H_4$ have been identified and their destruction and formation cross-sections determined. The apparent destruction cross-section was found to be a function of the electronic stopping power ($S_e$) as $\sigma_d \propto S_e^{3/2}$. The half-life of the $C_2H_2$ bombarded by galactic cosmic rays is estimated. The current findings are a contribution to the understanding of how the molecules synthesized upon irradiation of Interstellar and outer Solar system ices participate to the molecular enrichment and to the physicochemical evolution of the Universe.

**Key words:** astrochemistry – molecular data – methods: laboratory – interplanetary medium – cosmic rays – ISM: molecules.

## 1 INTRODUCTION

In space environment, volatile compounds can condense on dust grains creating precursor materials for stellar systems (Hollenbach & Thronson 1995). In the Solar system, ices can be found at the surface of satellites of outer planets, on trans-Neptunian objects, and in comets (Schmitt, de Bergh & Festou 1998; Barucci et al. 2008; Palumbo et al. 2008a). In the interstellar medium, icy species can be found in molecular clouds, dense regions where the temperature can be as low as 10 K (Tielens & Hagen 1982; Boogert, Gerakines & Whittet 2015). At these temperatures, atoms and molecules stick on to grain surfaces, forming an ice mantle coating (Gibb et al. 2004). In recent years, the understanding of the composition of interstellar

ice-covered grains and their importance to the chemico-physical evolution of the interstellar medium has increased. In this context, spectra of realistic laboratory analogues play a fundamental role (Strazzulla et al. 2002; Moore & Hudson 2005; Bennett et al. 2006).

Astrophysical ices exposed to the space environment undergo a variety of natural processes which may change their physicochemical properties. Most of these processes are irradiations, namely: electromagnetic radiation, bombardment by ions coming from the Sun (Solar wind), by galactic cosmic rays (GCR), or originated in planetary's magnetosphere (Prasad & Tarafdar 1983; Johnson 1990; Madey, Johnson & Orlando 2002; Gladstone 2012; Bennett, Pirim & Orlando 2013). Ion projectiles with energy within keV–GeV range transfer energy into these ices through elastic and inelastic collisions, breaking chemical bonds and inducing physicochemical modifications in the target. These modifications are structural (amorphyzation, crystallization, and/or compaction.) and may include synthesization of molecular species not present

★ E-mail: ana.barros@cefet-rj.br (ALFdB); enio@vdg.fis.puc-rio.br (EFdS)
† Present address: Max Planck Institute for Astronomy, Königstuhl 17, D-69117 Heidelberg, Germany.

**Table 1.** Experiment (irradiation) number, beam energy, ice layer thickness, deposition rate, fluence, irradiation time, electronic and nuclear stopping powers ($S_e$ and $S_n$, respectively), and penetration depth in $C_2H_2$ for each beam.

| Exp. | Beam | Energy (MeV) | Thickness ($\mu m$) | Deposition rate ($10^{-3}$ $\mu m\,s^{-1}$) | Maximum fluence ($10^{14}$ ions cm$^{-2}$) | Irradiation (h) | $S_e$ (keV $\mu m^{-1}$) | $S_n$ (keV $\mu m^{-1}$) | Penetration depth ($\mu m$) |
|---|---|---|---|---|---|---|---|---|---|
| 1 | $H^+$ | 1 | 0.55 | 4.6 | 4.6 | 21 | 30.4 | 0.22 | 21 |
| 2 | $He^+$ | 1 | 0.39 | 3.2 | 8.6 | 10 | 254 | 0.30 | 4.4 |
| 3 | $N^+$ | 1 | 0.30 | 2.5 | 1.9 | 8 | 775 | 9.23 | 1.9 |
| 4 | $N^+$ | 1.5 | 0.23 | 2.1 | 1.4 | 3 | 931 | 6.68 | 2.5 |
| 5 | $N^+$ | 1.5 | 4.0 | 6.0 | 4.9 | 20 | 931 | 6.68 | 2.5 |
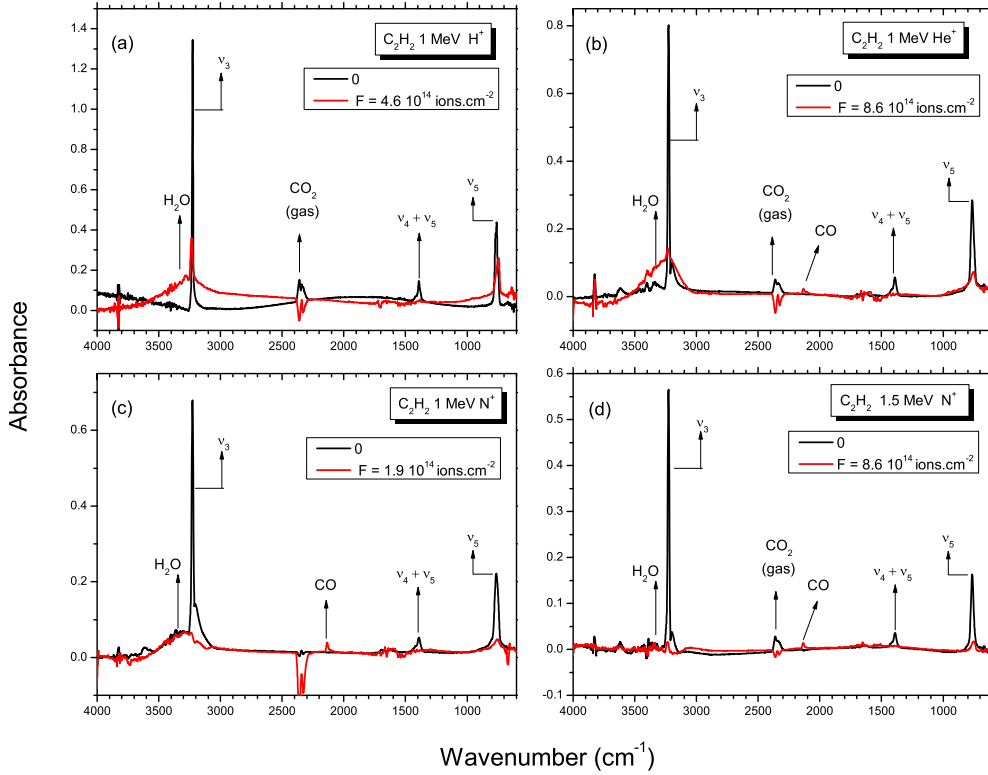


**Figure 1.** Infrared spectra of $C_2H_2$ ice, at 45 K, before and after irradiation. Ion beams: (a) 1 MeV $H^+$, (b) 1 MeV $He^+$, (c) 1 MeV $N^+$, and (d) 1.5 MeV $N^+$.

before the irradiation (Palumbo, Baratta & Spinella 2006; Palumbo et al. 2008b; Sivaraman et al. 2013; de Barros et al. 2016a; de Barros et al. 2016b, 2017; Pereira et al. 2018; Fulvio et al. 2019).

Concerning radiolysis by energetic particles, it is well known that the energy distribution of cosmic rays ranges from keV to MeV for the Solar wind (Lin, McGuire & Anderson 1974; Drury, Meyer & Ellison 1999), and from MeV to GeV for GCR (Drury et al. 1999; Shen et al. 2004). Protons are by far the most abundant; all the constituents have the maximum flux at a few keV/nucleon for the Solar wind, and at hundreds of MeV/nucleon for the GCR (e.g. Moore, Hudson & Gerakines 2001). Since this energy range is very difficult to be obtained in laboratory, our experiments were performed for MeV projectiles, based on the commonly accepted assumption that the impact effects are just scaled. Indeed, MeV/u to GeV/u interactions with matter occur mainly via ion-target electron collisions, in the so-called electronic stopping power regime. The consequence is that absolute cross-sections are different, but the physical phenomena involved are the same.

The acetylene molecule ($C_2H_2$) was detected in the interstellar medium, in gas phase, around young stellar objects and in molecular clouds (Lacy et al. 1989; Lahuis & van Dishoeck 2000; Carr & Najita 2008). In the Solar system, it has been found in the comae of some comets (Mumma et al. 1996, 2003; Magee-Sauer et al. 2002; Mumma & Charnley 2011). Additionally, it was also found as trace gas in Titan's stratosphere, and using Cassini Vims, its presence was reported at the surface of Titan in ice form (Lara et al. 1996; Coustenis et al. 1999; Singh et al. 2016); also, its occurrence on Triton and Pluto, diluted inside a dominant frozen nitrogen, has been suggested by Bohn et al. (1994). Due to the absence of a permanent dipole moment, $C_2H_2$ is not detectable by radio waves; its observation may be performed in the infrared range, although its strongest features in the solid phase are overlapped with the main $H_2O$ ice band (reminding that $H_2O$ is the dominant ice in interstellar regions; Knez et al. 2012). Solid phase $C_2H_2$ has been detected by *Spitzer*/IRS, through observation of stars behind dark molecular clouds, with abundance similar to the methane molecule ($CH_4$) (Knez et al. 2008).

In order to simulate the ice processing occurring in space, $C_2H_2$ was irradiated in its pure and mixture forms by ion beams (Hudson & Moore 1997, 2013; Moore & Hudson 1998), electrons (Zhou et al. 2010; Abplanalp et al. 2019), and photons (Gudipati et al. 2011; Ryazantsev, Zasimov & Feldman 2018; Bergner, Oberg
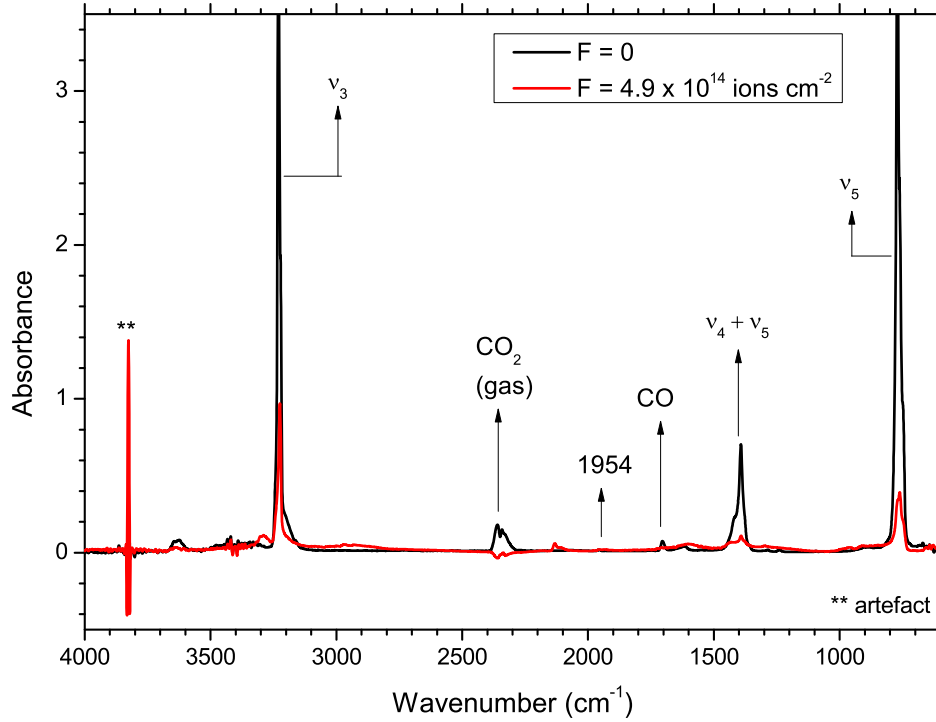
**Figure 2.** Spectra before and after irradiation of the thick film with 1.5 MeV N$^+$.

**Table 2.** Observed peak wavelengths, assignments, and intrinsic band strengths (*A*-values) for $C_2H_2$. Band positions currently found in literature are displayed for comparison.

| Band position (cm$^{-1}$) | Integration limits (cm$^{-1}$) | $\lambda$ ($\mu$m) | Mode | Assignment | *A*-value $10^{-18}$ cm molecule$^{-1}$ | Position (cm$^{-1}$) | Position (cm$^{-1}$) |
|---|---|---|---|---|---|---|---|
| 3225 | 3284–3176 | 3.10 | $\nu_3$ | CH stretch | $(16 \pm 1.5)^a$ | 3239$^a$ | 3224$^b$ |
| 1392 | 1483–1315 | 7.18 | $\nu_4 + \nu_5$ | $C_2H_2$ combination | $(2 \pm 1)^a$ | 1371$^a$ | 1393$^b$ |
| 1954$^c$ | 1968–1942 | 5.11 | – | as C≡C≡C stretch in –HC≡C≡CH$_2$ | $(0.03 \pm 0.01)^d$ | 1951$^e$ | 1951$^f$ |
| 761–771 | 813–690 | 13.1 | $\nu_5$ | CH bending | $(20 \pm 3)^a$ | 743$^a$ | 773$^b$ |

$^a$Knez et al. (2012).
$^b$Cuylle et al. (2014).
$^c$Observed only in the thick film.
$^d$Calculated in this work.
$^e$Zhou et al. (2010).
$^f$Abplanalp & Kaiser (2020).

& Rajappan 2019; Fleury et al. 2019; Krim & Jonusas, 2019; Zasimov et al. 2020), with different energies and temperatures. Cuylle et al. (2014) performed a systematic laboratory study of the VUV photochemistry of pure ice $C_2H_2$ irradiated at 12 K. They also irradiated ice mixtures of 100:1 Ar:$C_2H_2$ and 10:1 $H_2O$:$C_2H_2$.

Irradiation of hydrocarbons ($C_2H_2$, $C_2H_4$, $C_2H_6$), deposited at 12 K by 30 keV He$^+$ and 15 keV N$^+$ have been studied by Strazzulla et al. (2002). They found that, for ethylene, there are evidences of formation of new species, the most abundant being $CH_4$, $C_2H_6$, and $C_2H_2$. Also Kaiser et al. (1998) have irradiated $C_2H_2$ at 12 K by 9.0 MeV $\alpha$-particles and 7.3 MeV protons.

This work deals with the ion irradiation of solid $C_2H_2$ by 1.0 MeV H$^+$, 1.0 MeV He$^+$, 1.0 and 1.5 MeV N$^+$. Irradiated samples constituted by thin layers of $C_2H_2$ (i.e. with thicknesses much smaller than the penetration depth of the used projectiles) have been irradiated and analysed by Fourier transformed infrared (FTIR) spectroscopy. Moreover, 1.5 MeV N$^+$ ions have been used to irradiate $C_2H_2$ frozen layers with thickness larger than the penetration depth of the

incoming ions with the aim of better visualization the bands of the new molecules that are formed. The main objective of the current project is to simulate molecular synthesis induced by energetic light (or relatively light) ions constituents of the Solar wind and GCR.

## 2 EXPERIMENTAL SETUP

The experiments were performed at the Van de Graaff accelerator Laboratory of the Pontifical Catholic University at Rio de Janeiro (PUC-Rio), using ion beams at energies: 1.0 MeV H$^+$, 1.0 MeV He$^+$, and 1.0 and 1.5 MeV N$^+$.

A KBr substrate was previously introduced into the vacuum chamber and maintained at the desired pressure and temperature ($1 \times 10^{-8}$ mbar and 45 K). The $C_2H_2$ gas (purchased from Linde$^©$ with purity greater than 99 per cent) was injected into the chamber and deposited on the KBr substrate by condensation. The substrate temperature 45 K was chosen for avoiding $N_2$ and $O_2$ condensation on it during the runs.
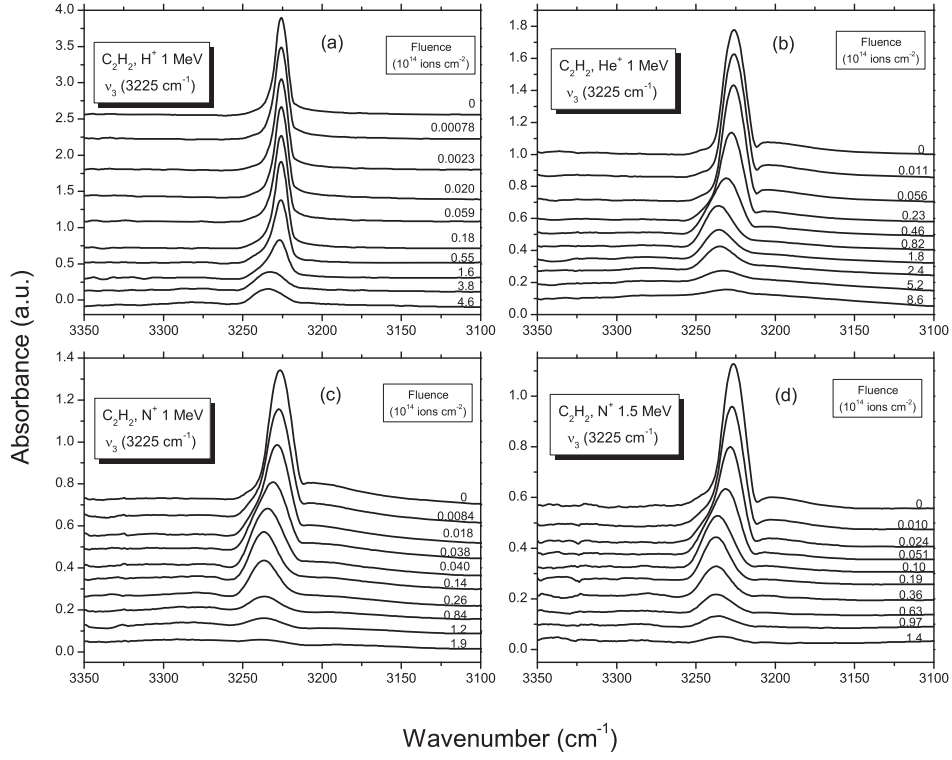
**Figure 3.** Infrared spectra for the $\nu_3$ band (3225 cm$^{-1}$) of C$_2$H$_2$ ice at 45 K for progressive beam fluences. Similar band modifications are observed for the four ion beams: blue shift and broader peak as the fluence increases.
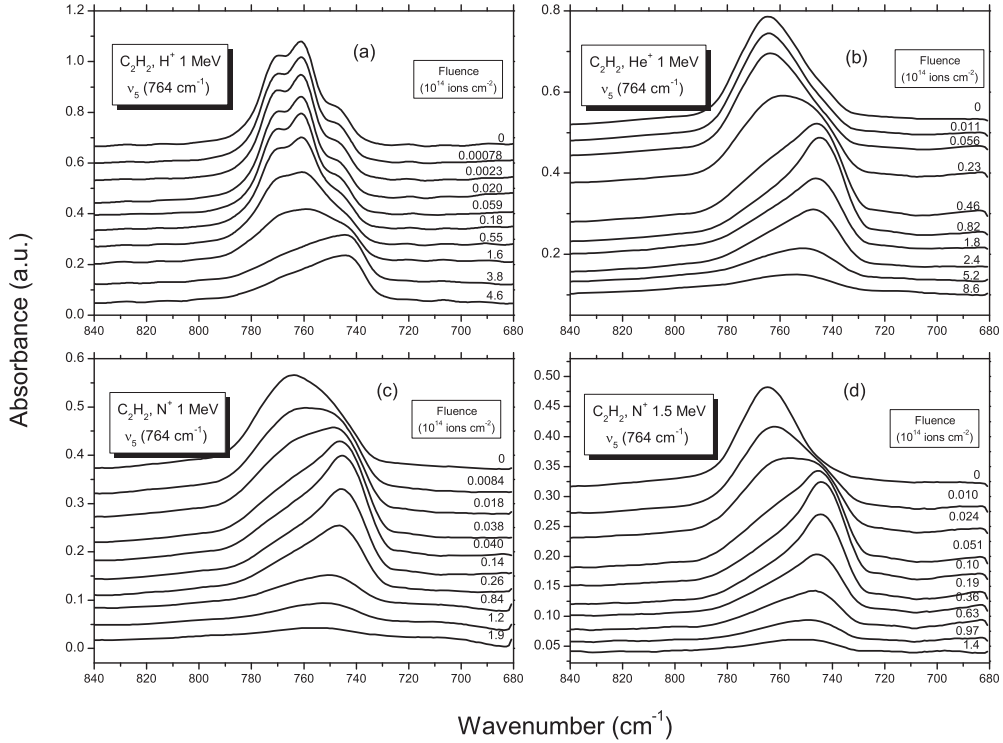
**Figure 4.** Infrared spectra for the $\nu_5$ band 764 cm$^{-1}$ of C$_2$H$_2$ ice at 45 K for several beam fluences. Similar band modifications are observed for the four ion beams: red shift and broader peak as the fluence increases.
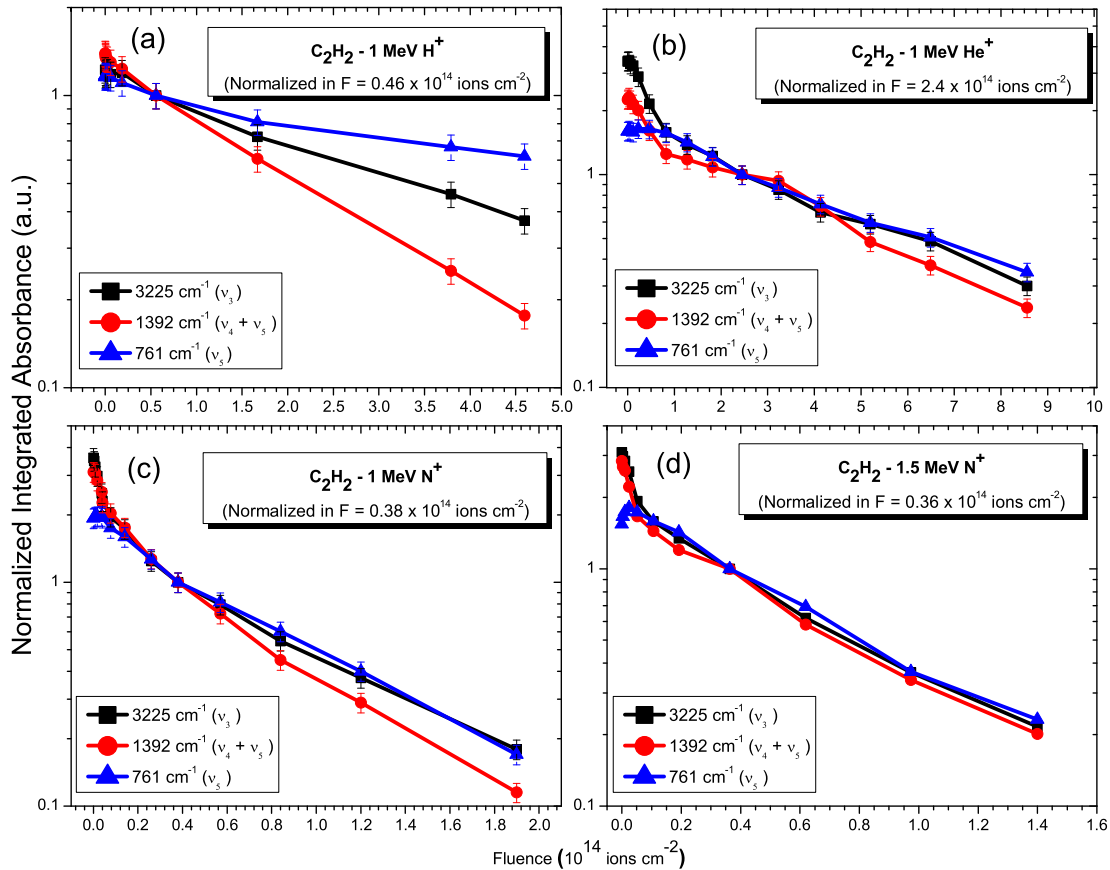
**Figure 5.** Evolution of the integrated absorbance with the beam fluence. Thin target irradiations: (a) 1 MeV H$^+$, (b) 1 MeV He$^+$, (c) 1 MeV N$^+$, and (d) 1.5 MeV N$^+$. For all bands, the integrated absorbance are normalized at the fluences indicated in each figure.

To obtain C$_2$H$_2$ thick films, the gas was deposited until the major bands ($\nu_3$ and $\nu_5$) were saturated, but leaving unsaturated the weak combination band $\nu_4 + \nu_5$ at 1392 cm$^{-1}$.

The thickness, $L$, of the sample (in μm) was determined by using equation (1); the values of the molar mass ($M$) and the mass density in the solid phase ($\rho$) of solid C$_2$H$_2$ used are 26.04 g mol$^{-1}$ and 1.16 g cm$^{-3}$, respectively. $N_0$ is the initial column density. Table 1 presents the thickness of the sample and the deposition rate (in μm s$^{-1}$) for each experiment performed.

$$L = \frac{N_0}{6.02 \times 10^{23}} \frac{M}{\rho} \times 10^4. \tag{1}$$

The ion beams impinged perpendicularly the ice target and their energies are listed in Table 1, as well as the ice layer thicknesses, deposition rate, fluence, irradiation time, electronic and nuclear stopping powers (S$_e$ and S$_n$), and the penetration depth in C$_2$H$_2$ for each beam. Note that the proton beam at 1 MeV has the highest penetration depth. Stopping powers have been calculated by the TRIM code (Ziegler, Ziegler & Biersack 2010). The penetration depths are much larger than the thicknesses of the samples for all experiments (with the exception of 1.5 MeV N$^+$ in Experiment 5). This indicates that for the four experiments with thin ice, the incident ions traverse the sample with small loss of velocity: collision cross-sections may be considered constant along the ion track of projectiles. For Experiment 5, performed with the thick ice, the implantation of N atoms occurs.

Fourier transform infrared spectroscopy (FTIR) was the analytical method used in this work. The molecular vibrational transitions

were observed with a JASCO 4200 – FTIR spectrometer, and each spectrum was acquired in the 4000–600 cm$^{-1}$ region, with 1 cm$^{-1}$ resolution.

## 3 RESULTS

### 3.1 C$_2$H$_2$ band analysis for thin ice target

Fig. 1 presents the full infrared spectra (4000–600 cm$^{-1}$) of C$_2$H$_2$ ice before and after the last irradiation with the following ions and energies: Fig. 1(a) for 1 MeV H$^+$, Fig. 1(b) for 1 MeV He$^+$, Fig. 1(c) for 1 MeV N$^+$, and Fig. 1(d) for 1.5 MeV N$^+$. Table 1 presents also the maximum fluence, the electronic and nuclear stopping powers and the predicted penetration depth for each of the four beams. For comparison, Fig. 2 shows the IR spectra for the thick target, acquired before and after irradiation with 1.5 MeV N$^+$; due to beam implantation in the beginning of irradiation, destruction cross-section varies during the slowing down.

Only four C$_2$H$_2$ vibrational bands are observed in the 4000–600 cm$^{-1}$ region: $\nu_3$ at 3225, 1954 cm$^{-1}$, $\nu_4 + \nu_5$ at 1392 cm$^{-1}$, and $\nu_5$ at approximately 764 cm$^{-1}$. Moderate variations in the peak shape (and therefore in the position of its maximum) are expected due to ice amorphyzation by the ion beam. Table 2 shows the characteristics of these C$_2$H$_2$ bands, as well as the integration limits used for the collection of their integrated absorbance and band strength values. Band positions are compared with those of the literature.
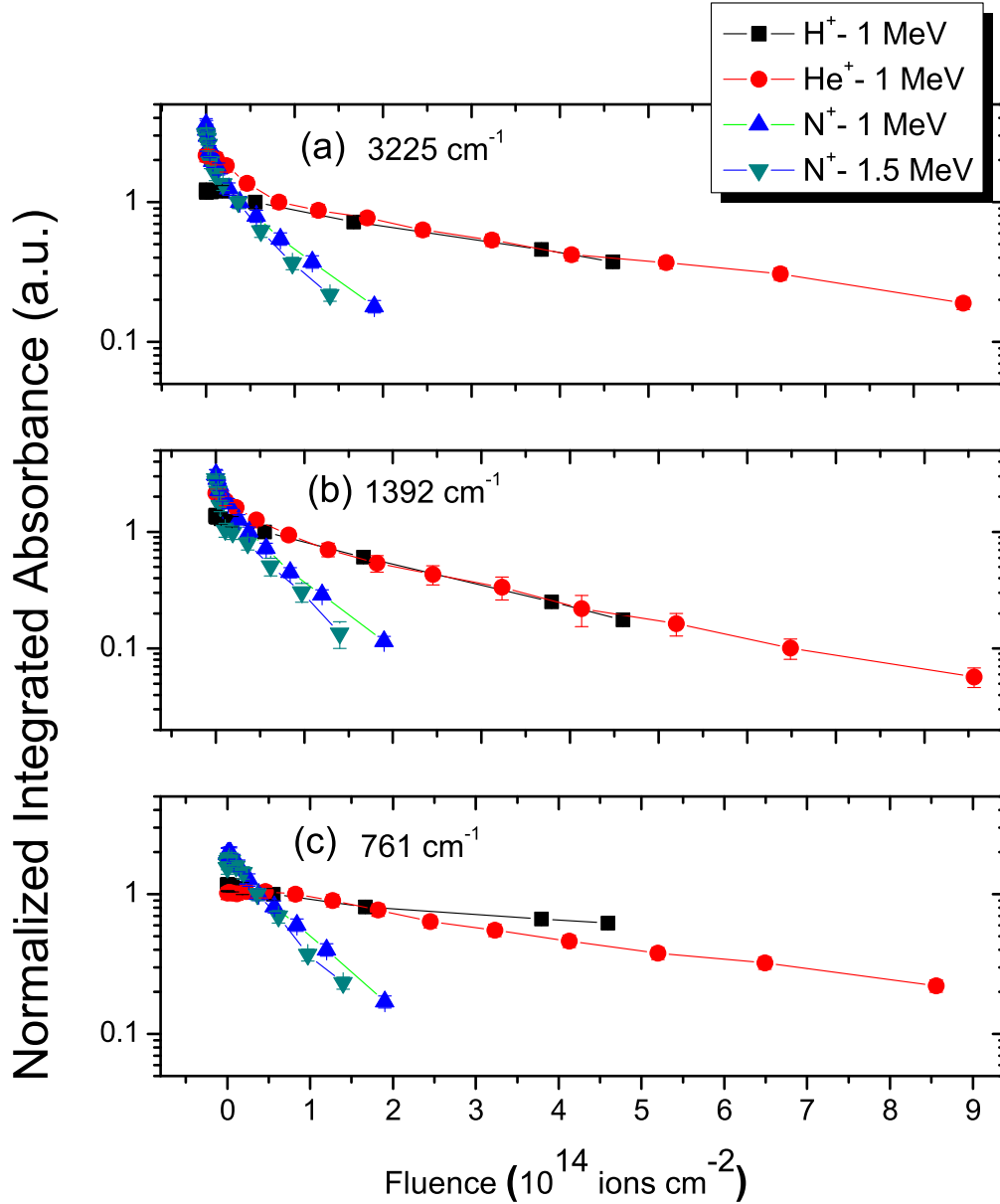
**Figure 6.** Comparison of the evolution of the integrated absorbance with different beams and fluence. The behaviors of the (a) 3225 cm$^{-1}$, (b) 1392 cm$^{-1}$, and (c) 761 cm$^{-1}$ bands are shown. For all bands, the integrated absorbance is normalized at the fluences indicated in Fig. 5.

Figs 3 and 4 show, respectively, the evolutions of $\nu_3$ and $\nu_5$ C$_2$H$_2$ bands for the four irradiations with thin targets. Relevant comments on these measurements are as follows:

(i) For the four thin film irradiations, three C$_2$H$_2$ bands were found: $\nu_3$ at 3225 cm$^{-1}$, $\nu_4 + \nu_5$ at 1392 cm$^{-1}$, and $\nu_5$ at 761 cm$^{-1}$.

(ii) For all the four experiments, the $\nu_3$ band exhibits blue-shifts, moving $\sim$10 cm$^{-1}$ towards the higher wave numbers. It occurs faster for the projectiles with larger stopping power, suggesting that the displacement is correlated with the ice compaction by the beam. The maximum displacement is of the order of 30 cm$^{-1}$ for the different beams used in the experiments.

(iii) Contrarily to the $\nu_3$ band, the $\nu_5$ band exhibits always a redshift. The maximum displacement is of the order of 15 cm$^{-1}$ for the different beams.

(iv) The $\nu_5$ band has a spectral structure more complex than the two other C$_2$H$_2$ bands visible in the spectra, being composed of at least three sub-bands: 770, 761, and 746 cm$^{-1}$; these sub-bands are clearly seen in the spectrum of the ice irradiated by H$^+$ (Fig. 4).

The band shift may be interpreted as a result of the evolution of the three sub-bands, each of them with a fixed wavenumber, but with an absorbance that changes differently from the others as the fluence increases. That is, along the irradiation, the absorbances of the bands at 770 and 762 cm$^{-1}$ decrease since the beginning, while the absorbance of the sub-band located at 746 cm$^{-1}$ shows an initial increase followed, as irradiation proceeds, by a decrease: this generates the displacement of the maximum of the envelope from 767 to 742 cm$^{-1}$.
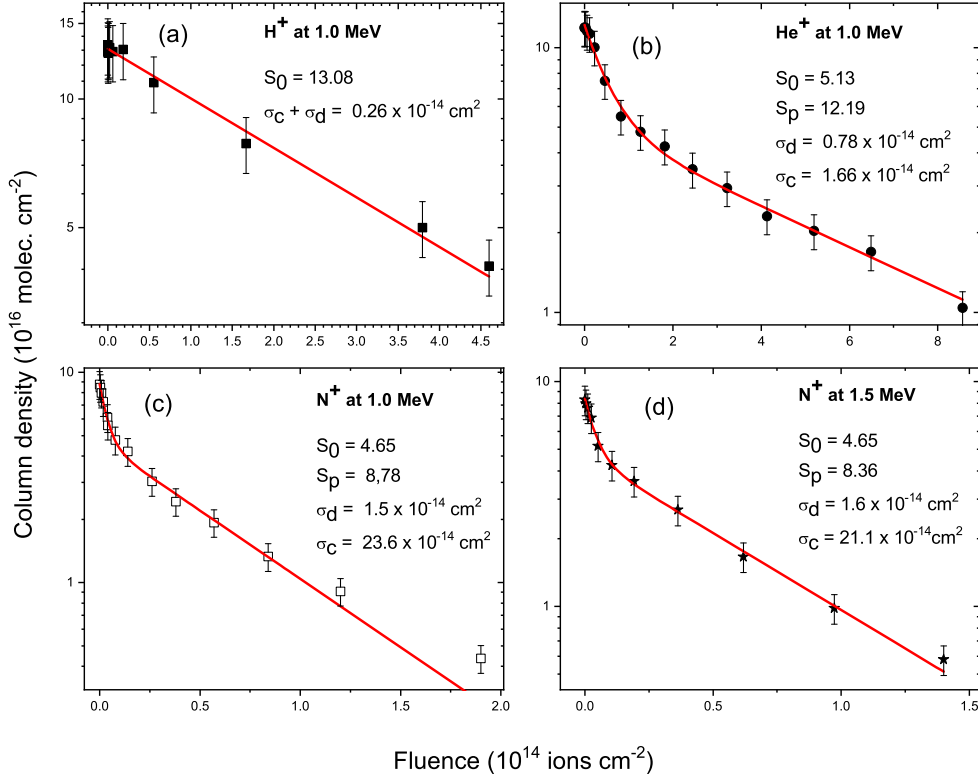
**Figure 7.** Dependence of the band 3225 cm$^{-1}$ of C$_2$H$_2$ absorbance on beam fluence. From the fittings (solid lines) with equation (2), the average destruction ($\sigma_d$) and compaction ($\sigma_c$) cross-sections for each beam are determined. Thin target irradiations data are here considered: (a) 1 MeV H$^+$, (b) 1 MeV He$^+$, (c) 1 MeV N$^+$, and (d) 1.5 MeV N$^+$.

**Table 3.** Initial integrated absorbance for compacted and porous ices, and cross-sections (in 10$^{-14}$ cm$^2$) for C$_2$H$_2$ ice irradiated by distinct ion beams. Data correspond to the 3225 cm$^{-1}$ band. $\sigma_d^{ap}$ is the apparent destruction cross-section; $\sigma_c$ is the compaction cross-section.

| Beam | Energy (MeV) | $S_0$ | $S_p$ | $\sigma_d^{ap}$ | $\sigma_c$ |
|------|------|------|------|------|------|
| H$^+$ | 1 | 13.1 | – | – | 0.26 |
| He$^+$ | 1 | 5.13 | 12.2 | 0.78 | 1.66 |
| N$^+$ | 1 | 4.65 | 8.78 | 1.5 | 23.6 |
| N$^+$ | 1.5 | 4.65 | 8.36 | 1.6 | 21.1 |

### 3.2 Phenomenological description: porous ices

Figs 3(a)–(d) and 4(a)–(d) display, respectively, the $\nu_3$ (3225 cm$^{-1}$) and $\nu_5$ (764 cm$^{-1}$) band spectra along the irradiation. Before irradiation, the measured integrated absorbance of the porous ice is called $S_p$. Once the irradiation starts, the band absorbance changes rapidly and – after a certain fluence – decreases exponentially with the decay parameter $\sigma_d^{ap}$ (Almeida et al. 2017).

Extrapolating the exponential behaviour down to $F = 0$, one gets the initial band integrated absorbance $S_0$. The absorbance variation, $S_0 - S_p$, is attributed to ice compaction. It turns out that the compaction process also evolves exponentially but with the decay parameter $\sigma_c$ (Mejía et al. 2013). The dependence of the band integrated absorbance, $S(F)$, on the ion beam fluence, $F$, is fitted fairly well by

$$S(F) = S_0 e^{-\sigma_d^{ap} F} - (S_0 - S_p)e^{-\sigma_c F}, \qquad (2)$$

where $\sigma_d^{ap}$ is the apparent destruction cross-section defined by the sum: $\sigma_d + Y_0/N_0$; $\sigma_d$ quantifies the chemical destruction (radiolysis); $Y_0/N_0$ is the sputtering ice factor, where $Y_0$ is the sputtering yield, caused by the ion bombardment and $N_0$ is the initial column density (Almeida et al. 2017).

Both processes, precursor radiolysis and sputtering, occur simultaneously and their rates are proportional to the local concentration of precursor molecules.

The second term in equation (2) describes absorbance variations due to structural accommodations of the ice, that is, compaction, crystallization, and amorphization. Strazzulla et al. (1992) and Leto & Barrata (2003) performed similar analysis for crystalline water ice amorphyzation. They have used the single exponential function $(1 - e^{-\sigma F})$ for quantifying the fraction of compacted ice. Here, it is reported that absorbance variation, $S_c(F)$, due to these accommodations, has its maximal value for the virgin ice ($S_0 - S_p$) and decreases exponentially with the compaction cross-section $\sigma_c$:

$$S_c(F) = (S_0 - S_p)e^{-\sigma_c F}. \qquad (3)$$

Fig. 5 shows the dependence of the integrated absorbance of the three C$_2$H$_2$ bands on the beam fluence observed for the four ion beams. For a better visualization of their behaviour with the fluence, the integrated absorbance are normalized at different fluences, depending on the experiment, when the compaction of the samples has been achieved. As shown in Fig. 5, all the three bands collapse practically into a single one, excepted for the 1 MeV H$^+$ beam (Fig. 5a). It can be seen that, for each irradiation, the integrated absorbance decreases exponentially, with rates close to each other, an evidence that distinct bands yield the same $\sigma_d^{ap}$.
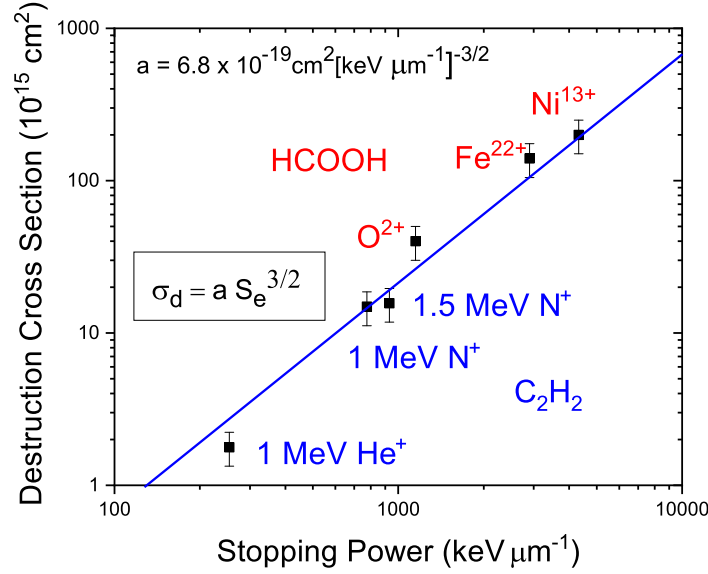
**Figure 8.** Dependence of the destruction cross-section on electronic stopping power. The solid line represents the power law $\sigma_d = a\,S_e^{3/2}$. The point corresponding to the 1 MeV H$^+$ irradiation is well above this empirical prediction, which is attributed to ice compaction rather than destruction (see the main text for further details).The three points relative to HCOOH data were taken from Andrade et al. (2013).

**Table 4.** Values of equation (4) parameters for distinct ice targets.

| Ice | $a$ $10^{-17}$ cm$^{-1}$ eV$^{-3/2}$ $(10^{15}$ molecules$)^{3/2}$ | $n$ | Reference |
|---|---|---|---|
| Aliphatic C–H | $a$ | (1.3) | Godard et al. (2011) |
| CH$_3$OH | $0.84 \pm 0.05$ | ∼3/2 | de Barros et al. (2011a, b) |
| CH$_4$ | 0.17 | ∼3/2 | Mejía et al. (2013) |
| HCOOH | $0.84 \pm 0.2$ | ∼3/2 | Andrade et al. (2013) |
| N$_2$O/N$_2$O:CO$_2$ | $1.6 \pm 2^b$ | ∼3/2 | Pereira et al. (2019) |
| C$_2$H$_2$ | $1.1 \pm 0.5$ | ∼3/2 | This work |

$^a a = 5\,(\pm 4)\,10^{-16}$ cm$^{-0.6}$ MeV$^{-1.3}$ mg$^{1.3}$.
$^b$Deduced from the reference.

It can be also seen in Fig. 5 that the compaction effects are perceived differently according to the band mode. Examined by the $\nu_3$ (CH-stretch) and $\nu_4 + \nu_5$ (C$_2$H$_2$ combination) modes, sample compaction decreases absorbance, that is, $S_c$ is negative. When analysed through the $\nu_5$ (CH-bending), the opposite occurs: $S_c$ is relatively low and positive ($S_0 > S_p$), meaning that this specific mode is less sensitive to compaction than the two others. A possible interpretation is that CH-stretch oscillations require more intermolecular space between the CH-bending vibrations, being therefore more affected by compaction.

The integrated absorbance evolutions for the three C$_2$H$_2$ bands and for each irradiation are presented in Fig. 5. Destruction and compaction cross-sections for each beam are determined by fitting these data with equation (3).

Fig. 6 shows the same data as Fig. 5 but displayed differently. The integrated absorbance evolutions of each band are now compared for the four different ion beams. It can be seen in Fig. 6(a), for the $\nu_3$ (3225 cm$^{-1}$) band, that H$^+$ and He$^+$ beams induce the same destruction rate. Comparing with the Figs 6(b) and (c), they have the same behaviour, differing with a little dispersion for the He$^+$ at higher fluence, in the $\nu_4 + \nu_5$ (1392 cm$^{-1}$) band.

The $\nu_3$ (3225 cm$^{-1}$) band was chosen, as reference, for the cross-section determination for the four experiments performed. Fig. 7 shows, for each irradiation, the fitting with equation (3) for the evolution of the integrated absorbance of the reference band as the fluence increases; note that only for the 1 MeV H$^+$ beam a single exponential is enough for a good fitting. This characteristic strongly suggests that the absorbance variations presented in Fig. 7(a) correspond predominantly to sample compaction process and not only to the C$_2$H$_2$ precursor destruction process.

Table 3 presents the values of the apparent destruction cross-sections ($\sigma_d^{ap}$), compaction cross-sections ($\sigma_c$), the initial integrated absorbance of the compacted ices ($S_0$) and the initial integrated absorbances of the porous ices ($S_p$) for the C$_2$H$_2$ $\nu_3$ band.

Fig. 8 shows the dependence of $\sigma_d^{ap}$ as a function of the electronic stopping power ($S_e$). The dependence of the destruction cross-section on the electronic stopping power is given by equation (4):

$$\sigma_d^{ap} = a S_e^n, \qquad (4)$$

where $a$ is a constant that depends on the type of the solid and $n$ is a parameter determined by the analysed data. Current data yield $a = 1.1 \times 10^{-17}$ cm$^{-1}$ eV$^{-3/2}$ $(10^{15}$ molecules$)^{3/2}$. A similar behaviour was already observed for other molecules; reported parameters are summarized in Table 4. The data here presented show that the exponent $n \sim 3/2$ in equation (4) describes correctly also for C$_2$H$_2$ ice the $\sigma_d^{ap}$ dependence on $S_e$. For comparison, three points relative to HCOOH cross-sections, taken from Andrade et al. (2013), are plotted in Fig. 8.

No band due to products was observed in the spectra acquired after the four irradiations with thin samples. Indeed, the absorbances of daughter molecules in these experiments were too low, near the baseline fluctuations.

### 3.3 Thick ice target: N$^+$ 1.5 MeV – beam implantation

To verify which daughter species could be formed by irradiating C$_2$H$_2$ ice samples, an additional experiment was then carried out with the 1.5 MeV N$^+$ ion beam, but with an ice film about 20 times
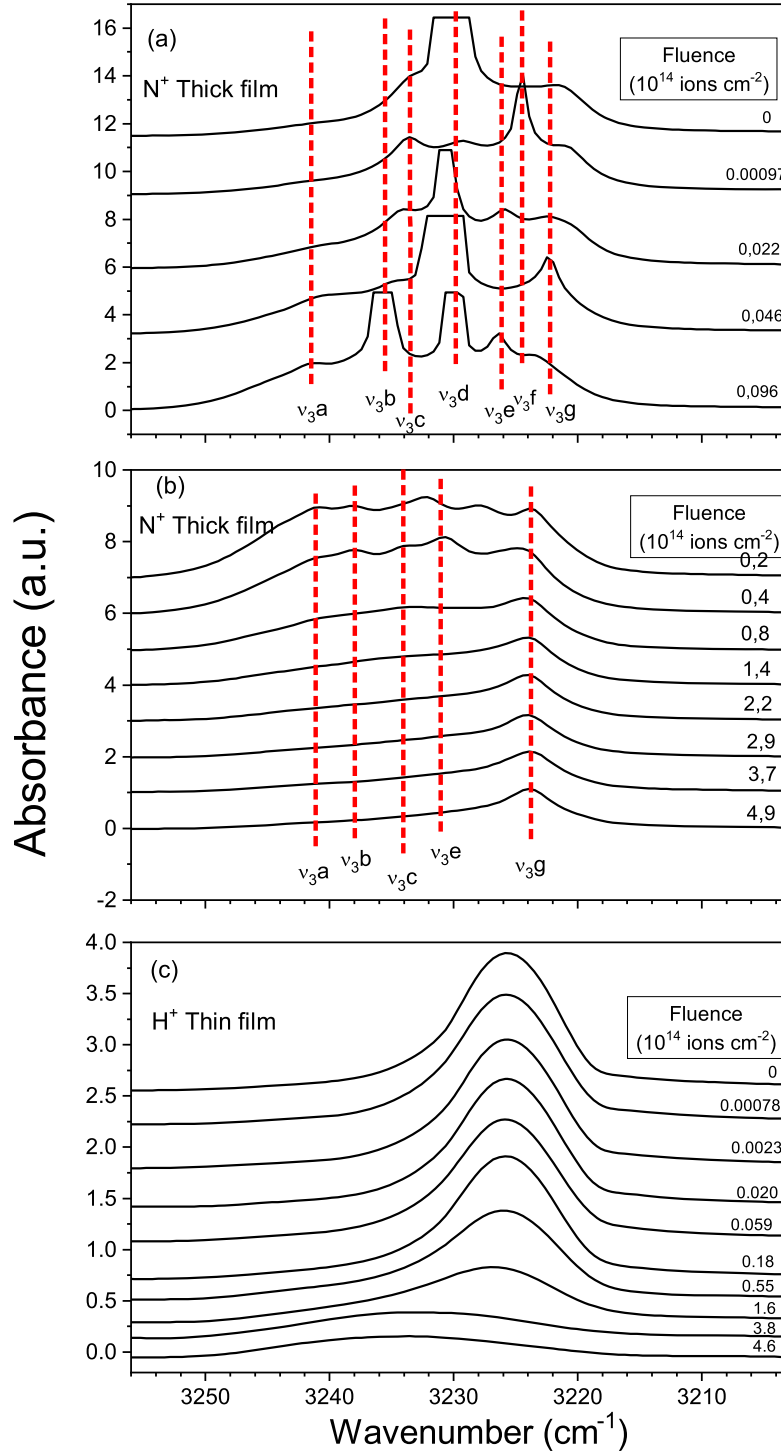
**Figure 9.** Evolution of the $\nu_3$ band with fluence. (a) The five first spectra of thick film irradiation by 1.5 MeV N$^+$, when the bands are still saturated; (b) spectra with unsaturated peaks for the same experiment; (c) spectra for thin film irradiated by 1.0 MeV H$^+$.

thicker than the previously ones . Fig. 2 presents the C$_2$H$_2$ spectra before and after irradiation. The weak 1954 cm$^{-1}$ band was seen in this thick ice (Table 2).

This beam was chosen for two reasons:

(i) Direct comparison with previous N$^+$ results;
(ii) N$^+$ beam has higher stopping power than H$^+$ and He$^+$ ones. It should be noted that thick ice films are very common in cosmic space, where grains, comet surfaces and asteroids are often covered with ice layers thicker than a few microns (typical penetration of MeV cosmic rays, see Table 1).

Since the penetration depth of 1.5 MeV N$^+$ in C$_2$H$_2$ is 2.5 µm (see Table 1), the projectiles get implanted at least at low fluences in a 4.0 µm thick ice. At high fluences, sputtering reduces the film thickness and the projectile gets implanted in the substrate. In

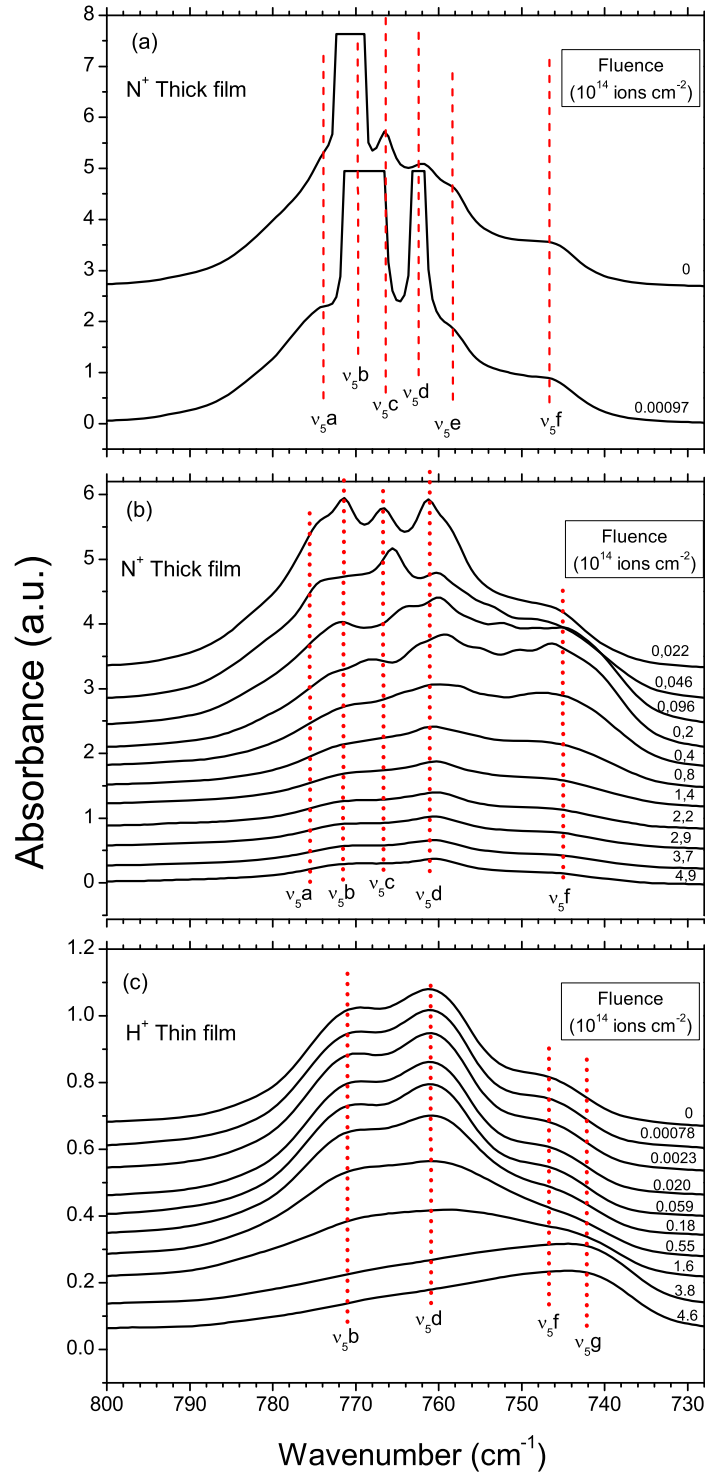**Figure 10.** Evolution of the $\nu_5$ band absorbance with fluence. (a) The two first spectra of thick film irradiation by 1.5 MeV N$^+$, when the bands are still saturated; (b) spectra with unsaturated peaks for the same run; (c) spectra for thin film irradiated by 1.0 MeV H$^+$.

general, the energy transfer from projectile to the sample occurs in a non-constant rate along the track.

Figs 9 and 10 compare the evolutions of $\nu_3$ and $\nu_5$ bands for the thick film bombarded by 1.5 MeV N$^+$ with those obtained for the 1 MeV H$^+$ irradiation on thin film. It can be seen that in the thick film experiment, the $\nu_3$ and $\nu_5$ bands are formed by a larger set of sub-bands, as tentatively listed in Table 5. Note

that these sub-bands show small variations in their wavelengths, possibly because the thick film is inhomogeneous. Moreover, the implantation of the beam inside the target leaves the rear part of the sample intact, keeping the characteristics of the virgin ice in this region.

The determination of the integrated absorbances for the $\nu_3$, $\nu_5$, and $\nu_4 + \nu_5$ bands of C$_2$H$_2$ was done by using the same integration

**Table 5.** Wavelengths in cm$^{-1}$ of the $\nu_3$ and $\nu_5$ sub-bands observed in the 1.5 MeV N$^+$ thick film irradiation. Positions of the saturated (∗) and non-saturated absorbance maxima of $\nu_5$ sub-bands are compared with the results of the thin film irradiated with 1.0 MeV H$^+$.

|   | Position $\nu_3$ 1.5 MeV N$^+$ | Position $\nu_5$ 1.5 MeV N$^+$ | Position $\nu_5$ 1.0 MeV H$^+$ |
|---|---|---|---|
| a | 3241 | 775 | – |
| b | 3238 | 771 | 770 |
| c | 3234 | 766 | – |
| d | 3229* | 761 | 761 |
| e | 3227 | 758* | – |
| f | 3224* | 746 | 746 |
| g | 3223 | – | 742 |

*Note.* (∗) Saturated bands.

limits as for the case of thin films irradiations (see Table 2). Fig. 11 shows the evolution of the integrated absorbance with the N$^+$ beam fluence. To preserve the correct evolution of the integrated absorbance, the experimental points corresponding to $\nu_3$ and $\nu_5$ bands of the saturated spectra (i.e. for initial fluences) were not placed in Fig. 11: for $\nu_5$ band, the considered data correspond to fluences $F > 2.17 \times 10^{12}$ ions cm$^{-2}$ and, for $\nu_3$ band, data are displayed for $F > 1.94 \times 10^{13}$ ions cm$^{-2}$. Integrated absorbances are normalized to unit at $F = 2.2 \times 10^{14}$ ions cm$^{-2}$.

Comparison of absorption evolution slopes of thin (Fig. 5) with thick (Fig. 11) film irradiations shows that the slope of the latter one is lower. This fact can be explained by the implantation of the N$^+$ beam in the sample which generates, at the beginning of the run, spectra with virgin and irradiated ice characteristics at the same time. To eliminate this effect, a subtraction of an integrated absorbance background was performed, taking the 4.44 cm$^{-1}$ band ($\nu_4 + \nu_5$) as reference. The integrated absorbance background value

was estimated to be 4.34 cm$^{-1}$ because it corresponds to the column density $N = 5.0 \times 10^{18}$ molecules cm$^{-2}$, which is the approximate column density of the non-irradiated region of the sample.

Results are presented in Fig. 12, which compares the absorbance evolution of the $\nu_4 + \nu_5$ band obtained in the experiment 1.5 MeV N$^+$ with the one of the same band with the baseline subtracted. The same absorbance rates indicate that despite the different sample thickness, the average destruction cross-sections are approximately equal.

Taking into account the background integrated absorbance, equation (2) was used to describe the dependence of the absorbance on the beam fluence. The values found for the destruction ($\sigma_d$) and compaction ($\sigma_c$) cross-sections are $1.6 \times 10^{-14}$ and $2.1 \times 10^{-13}$ cm$^2$, respectively (fitting in Fig. 12). Comparison between these values with those of 1.5 MeV N$^+$ beam irradiating thin targets (Table 3 or Fig. 12) shows that thick films exhibit slower average compaction.

### 3.4 Species synthesized by radiolysis (products)

Bands corresponding to products of C$_2$H$_2$ radiolysis were observed only for the thick film experiment. Indeed, for the thin films experiments, as already said before, the absorbances of new species produced by C$_2$H$_2$ radiolysis are too low and cannot been observed above the background. Fig. 13 shows obtained spectra before and during irradiation (up to $F = 4.9 \times 10^{14}$ ions cm$^{-2}$). The 3282 cm$^{-1}$ band may be classified as being the $\nu_1$ C$_4$H$_4$ band (Kim and Kaiser 2009). Three other C$_2$H$_4$ bands are seen in the analysed spectral range: $\nu_9$ at 3089 cm$^{-1}$, $\nu_{11}$ at 2971 cm$^{-1}$, and $\nu_{12}$ at 1435 cm$^{-1}$. The CH$_4$ $\nu_4$ band was identified at 1300 cm$^{-1}$ (de Barros et al. 2011a, b) and the C$_3$H$_6$ $\nu_{18}$ band coincides with the peak seen at 919 cm$^{-1}$ (Linstrom & Mallard 2001). All bands and their identification are
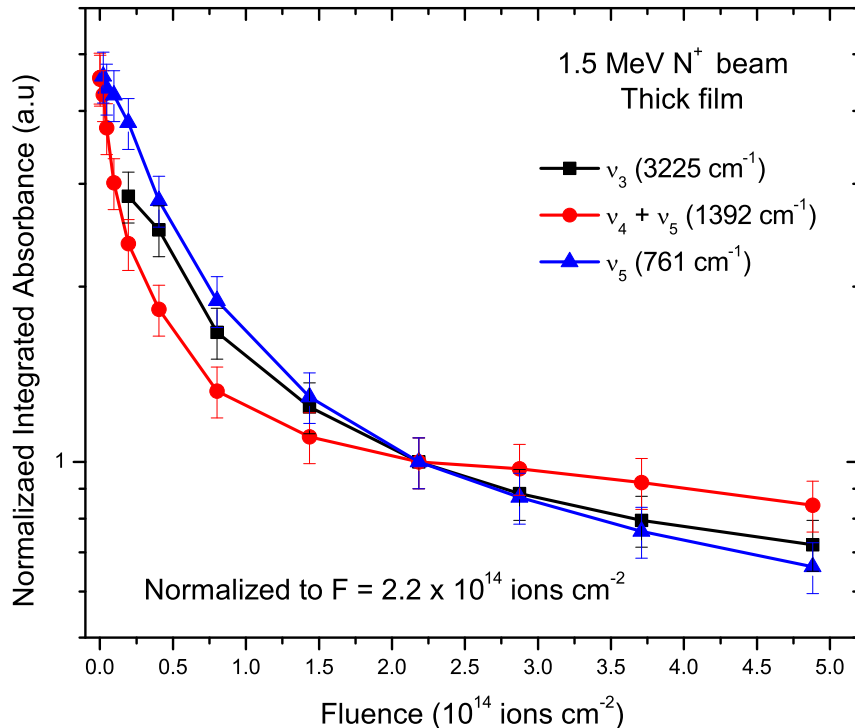


**Figure 11.** Evolution of integrated absorbance of the four observed bands of C$_2$H$_2$ irradiated with 1.5 MeV N$^+$ ion beam fluence. Data correspond to the thick film and are normalized to unit for $F = 2.2 \times 10^{14}$ ions cm$^{-2}$.
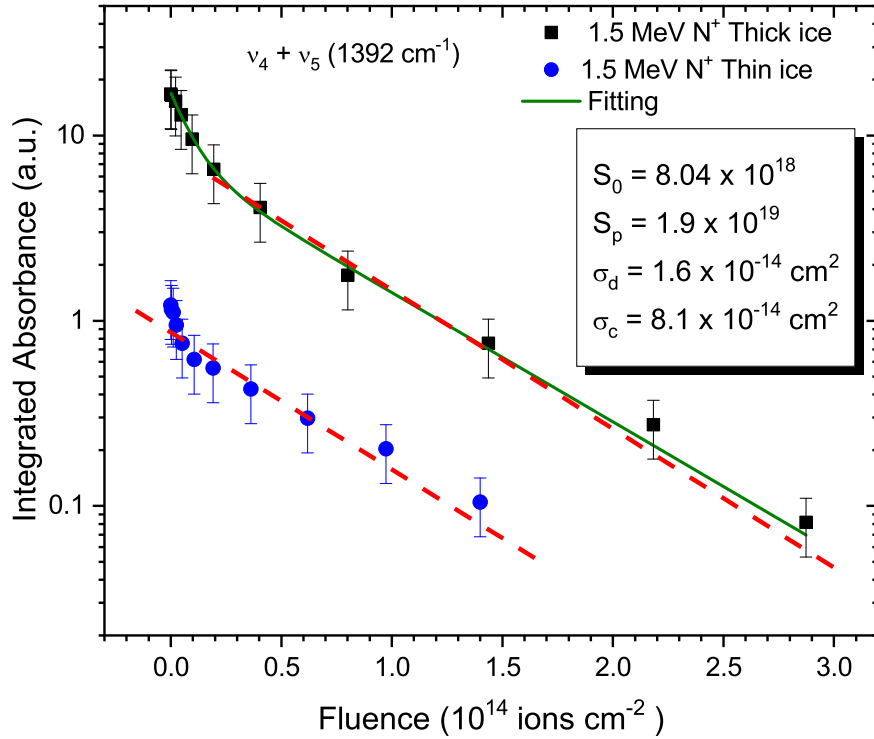
**Figure 12.** Comparison between the $\nu_4 + \nu_5$ band absorbance evolutions for the thick and thin ice experiments. 1.5 MeV $N^+$ ion beam was used for both irradiations. Solid line is fitting on the thick film band $\nu_4 + \nu_5$ using equation (2).

reported in Table 6. Table 7 shows the classification and attributions of the products $C_2H_4$ and $CH_4$.

The dependence of the column density on beam fluence for each of the three bands identified as belonging to $C_2H_4$ is presented in Fig. 14. It should be noted that the curves of the products, for both low and high fluences, show similar behaviour, as expected for bands of the same product.

The column densities of the product molecules are determined using equation (5), whose $A$-values ($A_\nu$) are listed in Table 6. They are assumed to be constant.

$$N = \frac{\ln 10 \int_{\nu_1}^{\nu_2} A(\nu) d\nu}{\int_{\nu_1}^{\nu_2} \varepsilon(\nu) d\nu} \equiv \ln 10 \frac{S(\nu)}{A_\nu}, \tag{5}$$

The column density evolution of each product is considered to follow equation (6), through which the destruction and formation cross-sections ($\sigma_{d,i}$ and $\sigma_{f,i}$) are extracted. The quantities $\sigma_d$ and $N_0$ of the precursor were obtained previously, namely $\sigma_d = 1.6 \times 10^{-14}$ cm$^2$ and $N_0 = 1.9 \times 10^{19}$ cm$^{-2}$.

$$N_i(F) \approx N_0 \sigma_{f,i} \left[ F - \frac{1}{2} (\sigma_{eff}) F^2 \right], \tag{6}$$

where $N_i(F)$ is the column density of the daughter species $i$ and $N_0$ is the initial column density of the precursor molecules from which the product originated: $\sigma_{f,i}$ is the formation cross-section and $\sigma_{eff} = \sigma_d + \sigma_{d,i}$ is the effective destruction cross-section for that daughter species; the quantities $\sigma_d$ and $\sigma_{d,i}$ are the precursor and product destruction cross-sections, respectively.

Fig. 15 shows the evolution of the $C_2H_4$ and $CH_4$ column densities, as determined from the indicated bands, during the $C_2H_2$ radiolysis. The solid curves are fittings obtained by using equation (6) and the formation and destruction cross-sections are displayed in Table 7. Since the $C_2H_4$ cross-sections are expected to

be the same regardless the band selected, the average cross-sections are also presented.

### 3.5 Analysis of contaminants

In ultra high vacuum analysis systems (residual pressures lower than $10^{-8}$ mbar), the usual contaminants in ice targets are $H_2$, $O_2$, $N_2$, $H_2O$, and $CO_2$. In general, $H_2$, $O_2$, and $N_2$ are mononuclear diatomic molecules, not active in the infrared (de Barros et al.2016a).

#### 3.5.1 CO₂

The IR spectrum acquired prior to irradiation (Figs 1 and 2) shows the presence of gas phase $CO_2$, well recognized by the 2334–2362 cm$^{-1}$ groups. Solid $CO_2$ produces a single asymmetric peak around 2344 cm$^{-1}$ (Isokoski, Poteet & Linnartz 2013); no clear signal in these two figures indicates the presence of solid $CO_2$. Another $CO_2$ band with peak centred at 1286 cm$^{-1}$ has been reported by Falk (1987) and by Isokoski et al. (2013). Again, no evident peak in the spectra suggests this band.

#### 3.5.2 H₂O

The common way to identify solid water is through its 3250 and 1650 cm$^{-1}$ bands. For all thin film irradiations (Fig. 3), a peak is seen growing at 3238 cm$^{-1}$, but it is narrower than a water band. For the thick film irradiation (Fig. 9), the 3238 cm$^{-1}$ band is associated to the $\nu_{3b}$ mode, whose absorbance decreases with fluence. Regarding the 1650 cm$^{-1}$ band, no clear indication of water is found although the region between 1750 and 1300 cm$^{-1}$ is somewhat noisy in the Fig. 1 spectra.
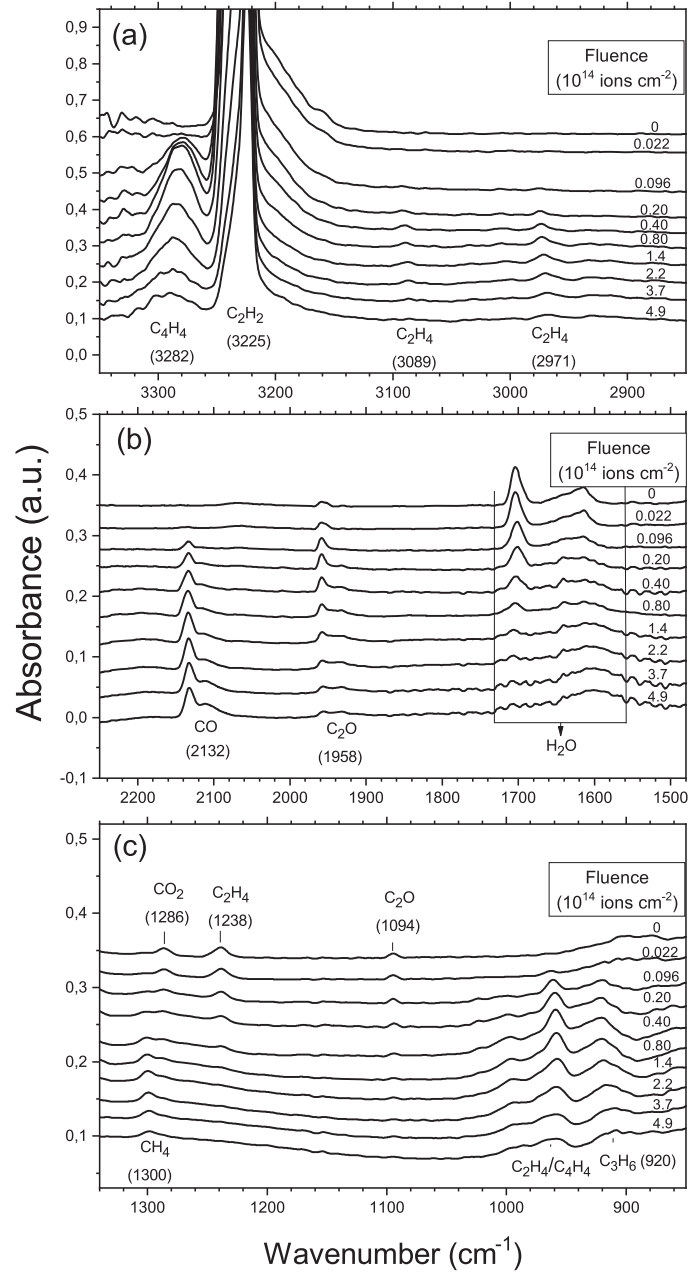
**Figure 13.** Infrared spectra of $C_2H_2$ ice, at 45 K, irradiated by 1.5 MeV $N^+$ for fluences from 0 to $4.9 \times 10^{14}$ ions $cm^{-2}$. Data correspond to (a) 3350 to 2850 $cm^{-1}$, (b) 2250 to 1480 $cm^{-1}$, and (c) 1340 to 850 $cm^{-1}$ spectral regions.

## 4 ASTROPHYSICAL IMPLICATIONS

In the Solar system, ices are found on the surface of satellites of outer planets, trans-Neptunian objects, and comets; in the interstellar medium, ices are found in molecular clouds, covering cosmic dust grains. Ices in space undergo a variety of natural processes, such as the ion processing induced by the Solar wind, GCR, or ions originated in planetary's magnetosphere. Energetic ions, when interacting with the ices, may transfer their energy into them through elastic and inelastic collisions, breaking chemical bonds, and inducing physicochemical modifications in the target. These modifications may include the synthesis of molecular species originally not present within the un-processed ices. It is therefore evident as the study of ices of astrophysical interest and their physicochemical evolution when exposed to ion processing is of great interest in the field of Planetary Sciences, Astrochemistry, and, to some extent, Astrobiology.

Acetylene is a species of astrophysical interest. As said in Section 1, it was already detected in the interstellar medium and in the Solar system. In solid phase, $C_2H_2$ was detected by *Spitzer*/IRS, through observation of stars behind dark molecular clouds (Knez et al. 2008) and, recently on Titan's surface (Singh et al. 2016). Also, when considering the daughter species ($CH_4$, $C_2H_4$, $C_3H_6$, and $C_4H_4$), formed during the thick film irradiation experiment, we want to point out that for $CH_4$ and $C_2H_4$, it was possible to determine their destruction and formation cross-sections. As for the case of acetylene, these two species are of particular astrophysical interest since they have been already detected in gas and solid

**Table 6.** IR band characteristics for the observed daughter species in thick film irradiation: assignment, wavenumbers in this work and in literature, and band strength ($A$-value).

| Molecule | Assignment | Wavenumber This work (cm$^{-1}$) | Wavenumber Literature (cm$^{-1}$) | Band strength ($10^{-18}$ cm molecule$^{-1}$) |
|---|---|---|---|---|
| $C_4H_4$ | $\nu_1$ | 3282 | 3284[a] | – |
| | $\nu_{14}/\nu_{15}$ | 978/(940) | 979/938[a] | – |
| $C_2H_4$ | $\nu_9$ | 3089 | 3095[b] | 2.2[b] |
| | $\nu_{11}$ | 2971 | 2974[c] | 6.0[c] |
| | $\nu_{12}$ | 1435 | 1436[b] | 3.1[b] |
| | $\nu_7$ | 959 | 951[c] | 15.0[d] |
| $CH_4$ | $\nu_4$ | 1300 | 1300[e] | 7.7[e] |
| $C_4H_2$ | $\nu_6 + \nu_9$ | 1238 | 1238[f] | – |
| $C_3H_6$ | $\nu_{13}$ | 919 | 919[g] | – |

[a]Kim and Kaiser (2009).
[b]Mejía et al. (2013).
[c]Cowieson, Barnes & Orville-Thomas (1981).
[d]Kaiser et al. (1998).
[e]de Barros et al. (2011a, b).
[f]Cuylle et al. (2014).
[g]Linstrom & Mallard (2001).

**Table 7.** Spectroscopic parameters of the $C_2H_2$ radiolysis products.

| Species | Position | $A_v$ | $\sigma_{f,i}$ | $\sigma_{d,i}$ |
|---|---|---|---|---|
| | (cm$^{-1}$) | ($10^{-18}$ cm molecule$^{-1}$) | ($10^{-16}$ cm$^2$) | ($10^{-16}$ cm$^2$) |
| $C_2H_4$ | 3089 | 2.2 | 3.2 | 87.0 |
| $C_2H_4$ | 2971 | 6.0 | 1.7 | 27.0 |
| $C_2H_4$ | 1435 | 3.1 | 1.9 | 53.0 |
| $C_2H_4$ average | – | – | 2.3 | 55.7 |
| $CH_4$ | 1300 | 7.7 | 0.26 | 19.0 |

phase in many different astrophysical environments, both in the ISM and the outer Solar system (see for instance the following references and those therein: Hanel et al. 1981; Cruikshank et al. 1993; Mumma et al. 1996; Schulz et al. 1999; Brown, Trujillo & Rabinowitz 2002; Gibb & Horne 2013; Grundy et al. 2016; Fonfría et al. 2017; McGuire 2018; Eistrup, Walsh & van Dishoeck 2019). Moreover, interestingly enough, methane has also been detected in exoplanetary atmospheres (Swain, Vasisht & Tinetti 2008; Stevenson et al. 2010; Barman et al. 2015).

The acetylene half-life in the ISM due to GCR bombardment can be estimated assuming:

(i) the molecule belongs to a thin film of $C_2H_2$ ice irradiated by GCR;
(ii) the GCR flux density is $d\Phi_j/dE = C_j E^{0.3}/(E + E_0)^3$, where $C_j$ is an abundance parameter characteristic of the GCR constituents ($j$ = H, He, C, O, Ne, and Fe, in this calculation), $E$ is the energy per nucleon and $E_0$ is a form parameter $\sim 400$ MeV (Shen et al. 2004);
(iii) the dependence on energy $E$ of the (apparent) destruction cross-section is $\sigma_{d,j}(E) = a\, S_e^{3/2}$.

The molecular disappearance is produced by radiolysis destruction and by sputtering; its rate is calculated using the apparent destruction cross-section. The disappearance rate due to the GCR constituent $j$ is $R_j = \int (d\Phi_j/dE)\, \sigma_{d,j}\, dE$.

Partial half-lives are calculated by $\tau_{1/2,j} = \ln(2)/R_j$ and the total half-life by $(\tau_{1/2})^{-1} = \Sigma_j (\tau_{1/2,j})^{-1}$. Results for $C_2H_2$ are presented in Fig. 16 and Table 8. Note that nevertheless H and He be the most abundant cosmic rays species, radiolysis and sputtering effects are ruled by Fe ions (Andrade et al. 2013; Dartois et al. 2013). This behaviour occurs because of the relative high Fe stopping powers and by its enhancement caused by the $\sigma_{d,j}(E) = a\, S_e^{3/2}$ law.

$C_2H_2$ half-life in the ISM is estimated to be $2 \times 10^8$ years. This result is comparable to the one predicted for HCOOH ice (Andrade et al. 2013) but, as estimated in the case of valine (da Costa et al. 2020), it is two orders of magnitude higher than those for larger molecules such as amino acids.

## 5 CONCLUSIONS

In this work, ice $C_2H_2$ has been irradiated by 1.0 MeV H$^+$, 1.0 MeV He$^+$, 1.0 and 1.5 MeV N$^+$. Two different ice thicknesses have been analysed: (i) samples constituted by a thin layer of $C_2H_2$ ice (i.e. with thickness shorter than the penetration depth of the projectile ions) and (ii) sample constituted by a thick layer of ice $C_2H_2$ (i.e. with thickness longer than the penetration depth of the projectile ions). By doing so, we had the possibility to focus on the physicochemical effects of ion irradiation, as a function of the irradiation fluence, in particular on (i) the evolution (destruction and compaction) of $C_2H_2$ and (ii) the evolution (formation and destruction) of the new molecules arising by $C_2H_2$ radiolysis (mainly $C_2H_4$ and $CH_4$), respectively.

Based on the results shown in the previous sections, the following conclusions can be highlighted:

(i) The main effect observed for the proton beam is ice compaction. However, for the current circumstances, radiolysis effects would overcome the compaction ones for an irradiation time at least three times longer. Removal rate by sputtering is comparable to destruction rate by radiolysis; the sum of the two effects is quantified by the apparent destruction cross-section, $\sigma_d^{ap}$. Occurrence of residual gas layering on the $C_2H_2$ ice reduces the sputtering yield but has negligible effect on radiolysis; in this case, $\sigma_d^{ap} \sim \sigma_d$.

(ii) The $\sigma_d^{ap} = a\, S_e^{3/2}$ approximate law, where $a = 6.8 \times 10^{-19}$ cm$^2$ (keV $\mu$m$^{-1}$)$^{-3/2}$, describes approximately the evolution of the data similarly to reported results for other ices.

Concerning the thick ice film irradiated by 1.5 MeV N$^+$:

(iii) Throughout the irradiation, the $\nu_3$ and $\nu_5$ $C_2H_2$ central bands exhibit a set of sub-bands having fixed vibrational positions but with relative absorbance that change considerably.

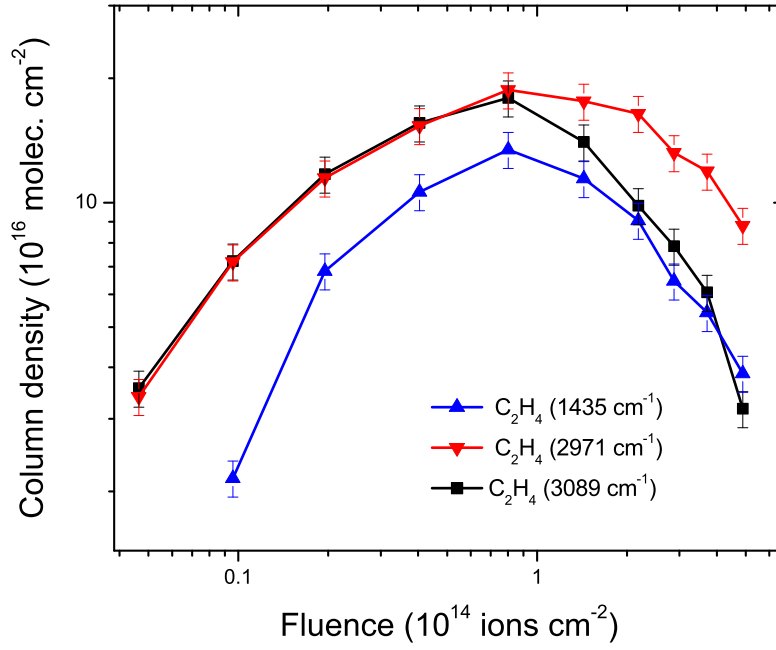(iv) Bands attributed to the products $C_4H_4$, $C_2H_4$, $CH_4$, and $C_3H_6$ have been observed.

**Figure 14.** Evolution of the $C_2H_4$, irradiated by 1.5 MeV $N^+$ ion beam, column density on fluence measured through its three observed bands.
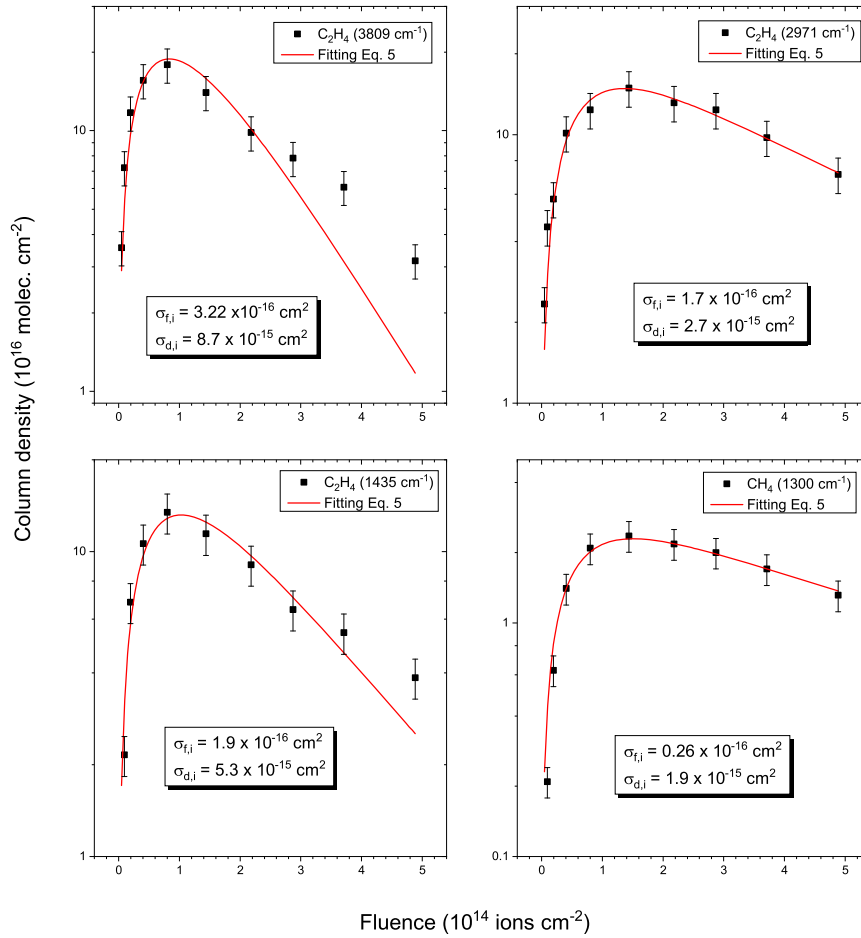


**Figure 15.** Evolution of the column densities of $C_2H_4$ and $CH_4$ produced by the radiolysis of $C_2H_2$, irradiated by 1.5 MeV $N^+$ ion beam. The solid curves are fittings obtained by equation (6).
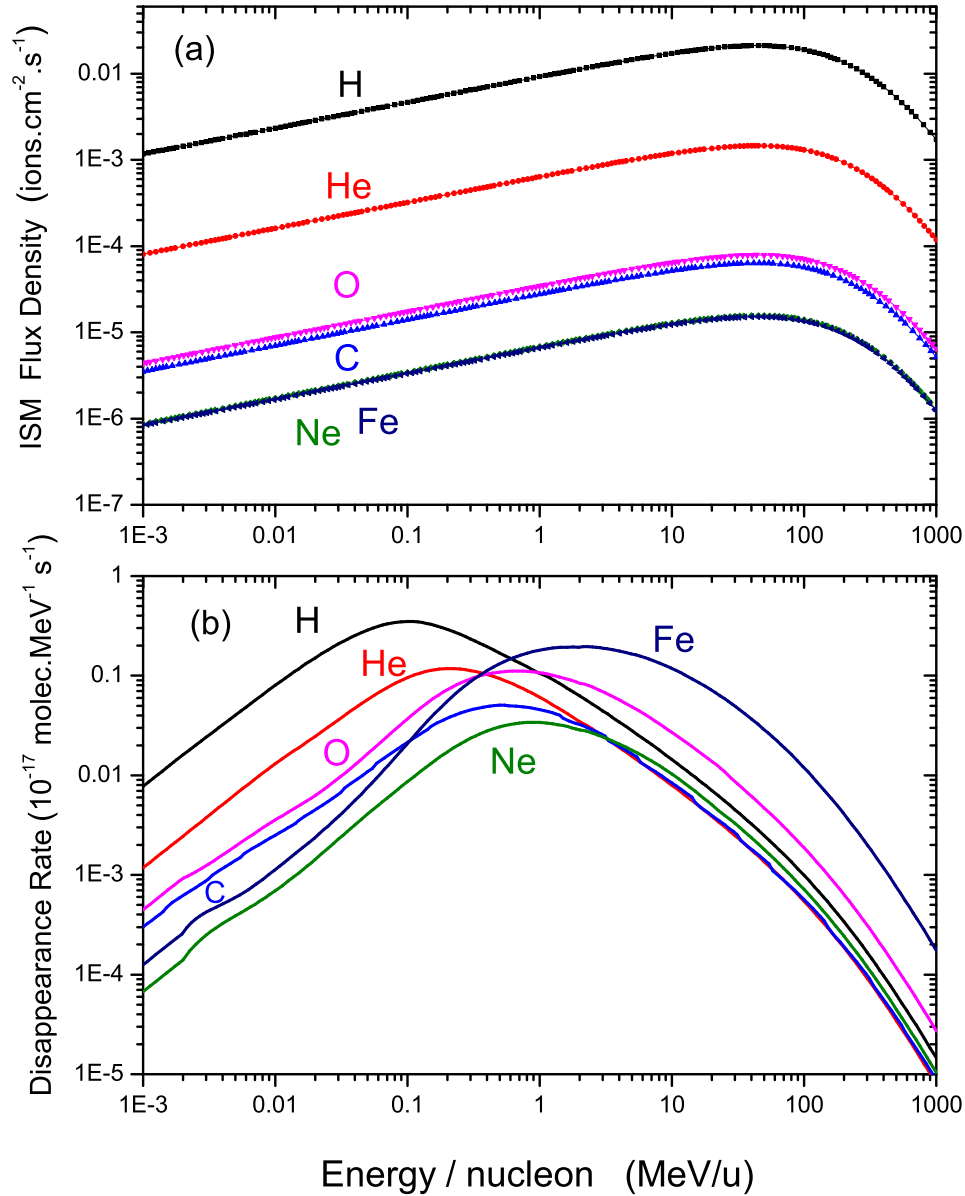
**Figure 16.** Energy dependence for the main cosmic ray constituents: (a) of the GCR flux density, according to Shen et al. (2004); (b) of the $C_2H_2$ disappearance rate density. Hydrogen and iron effect dominate the low and high GCR energies, respectively.

**Table 8.** Prediction of disappearance rates ($R_j$) and half-lives ($\tau_{1/2}$) due to each GCR species. $R_j$ is presented in second$^{-1}$ and giga-year$^{-1}$; $\tau_{1/2}$ is shown in giga-year.

| $j$ | $R_j$ (molecule $10^{-16}$ s$^{-1}$) | $R_j$ (molecule Ga$^{-1}$) | $\tau_{1/2}$ (Ga) |
|---|---|---|---|
| H | 0.088 | 0.28 | 2.5 |
| He | 0.047 | 0.15 | 4.7 |
| C | 0.043 | 0.13 | 5.1 |
| O | 0.13 | 0.41 | 1.7 |
| Ne | 0.047 | 0.15 | 4.6 |
| Fe | 0.59 | 1.9 | 0.37 |
| Total | 0.94 | 3.0 | 0.23 |

(v) The formation cross-sections of the $C_2H_4$ and $CH_4$ produced by $C_2H_2$ radiolysis are $2.4 \times 10^{-16}$ and $2.6 \times 10^{-17}$ cm$^2$, respectively, and their destruction cross-sections, $5.1 \times 10^{-15}$ and $1.9 \times 10^{-15}$ cm$^2$.

(vi) $C_2H_2$ half-life in the ISM is predicted to be $2 \times 10^2$ Ma (million years), value to be compared to $3 \times 10^2$ Ma for formic acid ice (Andrade et al. 2013) or to 1 Ma for solid valine (da Costa et al. 2020).

This work originates from a long-term laboratory project where the main purpose is to simulate and study the effects of Solar wind, GCR, and ions originated in planetary's magnetosphere on interstellar and outer Solar system ices. Here, we have presented the results of ion irradiation of ice $C_2H_2$. These results should contribute to our comprehension of the physicochemical evolution of the Universe.

**REFERENCES**

Abplanalp M. J., Kaiser R. I., 2020, ApJ, 889, 26
Abplanalp M. J., Frigge R., Kaiser R. I., 2019, Sci. Adv., 5
Almeida G. C., Pilling S., de Barros A. L. F., da Costa C. A. P., Pereira R. C., da Silveira E. F., 2017, MNRAS, 471, 1330
Andrade D. P., de Barros A. L., Pilling S., Domaracka A., Rothard H., Boduch P., da Silveira E. F., 2013, MNRAS, 430, 787
Barman T. S., Konopacky Q. M., Macintosh B., Marois C., 2015, ApJ, 804, 61
Barucci M. A., Boehnhardt H., Cruikshank D. P., Morbidelli A., 2008, The Solar System Beyond Neptune. Univ. Arizona Press, Tucson, AZ
Bennett C. J., Jamieson C. S., Osamura Y., Kaiser R. I., 2006, ApJ, 653, 792
Bennett C. J., Pirim C., Orlando T. M., 2013, Chem. Rev., 113, 9086
Bergner J. B., Oberg K. I., Rajappan M., 2019, ApJ, 874, 115
Bohn R. B., Sandford S. A., Allamandola L. J., Cruikshank D. P., 1994, Icarus, 111, 151
Boogert A. C. A., Gerakines P. A., Whittet D. C. B., 2015, ARA&A, 53, 541
Brown M. E., Trujillo C. A., Rabinowitz D. L., 2005, ApJ, 635, L97
Carr J. S., Najita J. R., 2008, Science, 319, 1504
Coustenis A., Schmitt B., Khanna R. K., Trotta F., 1999, Planet. Space Sci., 47, 1305
Cowieson D. R., Barnes A. J., Orville-Thomas W. J., 1981, J. Raman Spectrosc., 10, 224
Cruikshank D. P., Roush T. L., Owen T. C., Geballe T. R., De Bergh C., Schmitt B., Bartholomew M. J., 1993, Science, 261, 742
Cuylle S. H., Zhao D., 2014, A&A, 570, A83
da Costa C. A., Muniz G. S. V., Boduch P., Rothard H., da Silveira E. F., 2020, Int. J. Mol. Sci., 21, 1893
Dartois E., Ding J. J., De Barros A. L. F., Boduch P., Brunetto R., Chabot M., Pino T., 2013, A&A, 557, A97
de Barros A. L. F., Domaracka A., Andrade D. P. P., Boduch P., Rothard H., da Silveira E. F., 2011a, MNRAS, 418, 1363
de Barros A. L. F., Bordalo V. S. D. E., Duarte E. S., da Silveira E. F., Domaracka A., Rothard H., Boduch P., 2011b, A&A, 531, A160
de Barros A. L. F., da Silveira E. F., Fulvio D., Boduch P., Rothard H., 2016a, MNRAS, 465, 3281
de Barros A. L. F., da Silveira E. F., Fulvio D., Rothard H., Boduch P., 2016b, ApJ, 824, 81
de Barros A. L. F., da Silveira E., Fulvio D., Boduch P., Rothard H., 2017, MNRAS, 465, 3281
Drury L. O. C., Meyer J. P., Ellison D. C., 1999, in DuVernois M. A., ed., Topics in Cosmic-Ray Astrophysics. Nova Science Publishers, New York, p. 171
Eistrup C., Walsh C., van Dishoeck E. F., 2019, A&A, 629, A84
Falk M., 1987, J. Chem. Phys., 86, 560
Fleury B., Gudipati M. S., Couturier-Tamburelli I., Carrasco N., 2019, Icarus, 321, 358
Fonfría J. P., Hinkle K. H., Cernicharo J., Richter M. J., Agndez M., Wallace L., 2017, ApJ, 835, 196
Fulvio et al., 2019, MNRAS, 483, 381
Gibb E. L., Horne D., 2013, ApJ, 776, L28
Gibb E. L., Whittet D. C. B., Boogert A. C. A., Tielens A. G. G. M., 2004, ApJS, 151, 35
Gladstone G. R. et al., 2012, J. Geophys. Res., 117, 12
Godard M., Féraud G., Chabot M., Carpentier Y., Pino T., Brunetto R., Dartois E., 2011, A&A, 529, A146

Grundy W. M., Binzel R. P., Buratti B. J., Cook J. C., Cruikshank D. P., Dalle Ore C. M., Olkin C. B., 2016, Science, 351, aad9189
Gudipati M. S., Jacovi R., Lignell A., Couturier I., 2011, Condensed-Phase Photochemical Processes in Titan's Aerosols and Surface: The Role of Longer Wavelength Photochemistry Vol. 6, EPSC-DPS2011
Hanel R., Conrath B., Flasar F. M., Kunde V., Maguire W., Pearl J., Cruikshank D., 1981, Science, 212, 192
Hollenbach D. J., Thronson H. A., 1995, Interstellar Processes, Ist edn. D. Reidel Publishing Company, Dordrecht, Holland
Hudson R. L., Moore M. H., 1997, Icarus, 126, 233
Hudson R. L., Moore M. H., 2013, ApJ, 773, 109
Isokoski K., Poteet C. A., Linnartz H., 2013, A&A, 555, A85
Johnson R. E., 1990, Energetic Charged Particle Interactions with Atmospheres and Surfaces, 1st edn. Springer-Verlag, Berlin
Kaiser R. I., Roessler K., 1998, ApJ, 503, 959
Kim Y. S., Kaiser R. I., 2009, ApJS, 181, 543
Knez C. et al., 2008, in Kwok S., Sandford S., eds, IAU Symp.Vol. 251, Organic Matter in Space. Cambridge Univ. Press, Cambridge, p. 47
Knez C., Moore M. H., Ferrante R. F., Hudson R. L., 2012, ApJ, 748, 95
Krim L., Jonusas M., 2019, Low Temp. Phys., 45, 606
Lacy J. H., Evans N. J., Achtermann J. M., Bruce D. E., Arens J. F., Carr J. S., 1989, ApJ, 342, L43
Lahuis F., van Dishoeck E. F., 2000, A&A, 355, 699
Lara L. M., Lellouch E., López-Moreno J. J., Rodrigo R., 1996, J. Geophys. Res., 101, 23261
Leto G., Baratta G. A., 2003, A&A, 397, 7
Lin R. P., McGuire R. E., Anderson K. A., 1974, in Newkirk G., Jr, ed., Proc. IAU Symp. Vol. 57, Coronal Disturbances. International Astronomical Union, Paris, p. 461
Linstrom P. J., Mallard W. G., 2001, NIST Chemistry Webbook; NIST Standard Reference Database No. 69
McGuire B. A., 2018, ApJS, 239, 17
Madey T. E., Johnson R. E., Orlando T. M., 2002, Surf. Sci., 500, 838
Magee-Sauer K. et al., 2002, ESA SP-500: Production of HCN and $C_2H_2$ in Comet C/2002 C1 Ikeya-Zhang in Asteroids, Comets, and Meteors. ESA, Noordwijk, p. 549
Mejía C. F., de Barros A. L. F., Bordalo V., da Silveira E. F., Boduch P., Domaracka A., Rothard H., 2013, MNRAS, 433, 2368
Moore M. H., Hudson R. L., 1998, Icarus, 135, 518
Moore M. H., Hudson R. L., 2005, Proc. IAU Symp. Vol. 231, Astrochemistry: Recent Successes and Current Challenges. p. 247
Moore M. H., Hudson R. L., Gerakines P. A., 2001, Spectrochim. Acta A: Mol. Biomol. Spectrosc., 57, 843
Mumma M. J., Charnley S. B., 2011, ARA&A, 49, 471
Mumma M. J. et al., 1996, Science, 272, 1310
Mumma M. J., DiSanti M. A., Russo N. D., Magee-Sauer K., Gibb E., Novak R., 2003, Adv. Space Res., 31, 2563
Palumbo M. E., Baratta G. A., Spinella F., 2006, Mem. Soc. Astron. Ital. Suppl., 9, 192
Palumbo M. E. et al., 2008a, J. Phys.: Conf. Ser., 101, 012002
Palumbo M. E., Baratta G. A., Fulvio D., Garozzo M., Gomis O., Leto G., Spinella F., Strazzulla G., 2008b, J. Phys.: Conf. Ser., 101, 012002
Pereira R. C., de Barros A. L. F., Fulvio D., Boduch P., Rothard H., da Silveira E. F., 2018, MNRAS, 478, 4939
Pereira R. C., de Barros A. L. F., Fulvio D., Boduch P., Rothard H., da Silveira E. F., 2019, Nuclear Instruments and Methods in Physics Research Section B: Beam Interactions with Materials and Atoms, 460, 249
Prasad S. S., Tarafdar S. P., 1983, ApJ, 267, 603
Ryazantsev S. V., Zasimov P. V., Feldman V. I., 2018, X-ray Radiolysis of $C_2$ Hydrocarbons in Cryogenic Media Radiation Physics and Chemistry, Vol. 151, Elsevier. p. 253
Schmitt B., de Bergh C., Festou M., 1998, Solar system Ices, Astrophysics Space Science Library, Vol. 227, Springer, Berlin, p. 118
Schulz B., Encrenaz T., Bézard B., Romani P. N., Lellouch E., Atreya S. K., 1999, Detection of C2H4 Neptune from ISO/PHT-S Observations, Vol.31, American Astronomical Society, p. 1180

Shen C. J., Greenberg J. M., Schutte W. A., van Dishoeck E. F., 2004, A&A, 415, 203

Singh S. et al., 2016, ApJ, 828, 55

Sivaraman B. et al., 2013, J. Chem. Phys., 139, 074706

Stevenson K. B., Harrington J., Nymeyer S., Madhusudhan N., Seager S., Bowman W. C., Lust N. B., 2010, Nature, 464, 1161

Strazzulla G., Baratta G. A., Leto G., Foti G., 1992, Europhys. Lett., 18, 517

Strazzulla G., Baratta G. A., Domingo M., Satorre M. A., 2002, Phys. Res. B, 191, 714

Swain M. R., Vasisht G., Tinetti G., 2008, Nature, 452, 329

Tielens A. G. G. M., Hagen W., 1982, A&A, 114, 245

Zasimov P. V., Ryazantsev S. V., Tyurin D. A., Feldman V. I., 2020, MNRAS, 491, 5140

Zhou L., Zheng W., Kaiser R. I., Landera A., Mebel A. M., Liang M., Yung Y. L., 2010, ApJ, 718, 1243

Ziegler J. F., Ziegler M. D., Biersack J. P., 2010, Nucl. Instrum. Methods Phys. Res. B, 268, 1818689

This paper has been typeset from a TeX/LaTeX file prepared by the author.